

# Simulations of turbulence screens for flow and noise control in tandem cylinders

Wenqing Zhu\*, Zhixiang Xiao\*<sup>†</sup>, and Song Fu\*

\*School of Aerospace Engineering, Tsinghua University  
Beijing, 100084, China

Email: xiaotigerzhx@tsinghua.edu.cn

<sup>†</sup>Corresponding author

## Abstract

Flow and noise controls by turbulence screens were numerically modeled by introducing source terms into Navier-Stokes equations. This model was validated by several cases. Good agreements with theories or measurements were achieved, including the resistance and deflection coefficients, turbulence reduction factors, and time-averaged velocities. Then, it was applied to control flows past the tandem cylinders. Present model can predict the reduction of velocity and fluctuations on the rear cylinder. A drastic noise reduction was also obtained. The screen with porosity of 0.66 achieved a maximum reduction of 4.9 dB at the emission angle of 120°.

## 1. Introduction

Landing gear is an important airframe-noise source of a commercial airplane at the stage of landing<sup>1</sup>. It needs to be significantly reduced to meet the more stringent noise regulation. There are many unfriendly aerodynamic or acoustic components in a real landing gear, such as wheels, struts, rocker arms, and so on. They are very noisy and hard to perform the acoustic optimization owing to their main functions.

Shielding these components with fairings is an effective method to control the landing gear noise<sup>2</sup>. Perforated fairings have been conducted and demonstrated an impressive noise reduction<sup>3,4</sup>. Turbulence screens and perforated fairings are similar in shape, so they may have similar functions in flow control. Actually, the turbulence screens have been used as flow control devices to reduce velocity fluctuations or turbulence levels<sup>5</sup> in many industrial applications, such as the pipe, wind tunnel, and so on. The turbulence screens have been investigated as noise control strategies to reduce the airframe noise in several international cooperation projects, such as Technologies to IMProve Airframe Noise (TIMPAN) and Innovative Methodologies and technologies for reducing Aircraft noise Generation and Emission (IMAGE). For the strut tested in the TIMPAN project, a lateral elliptic screen yielded a great broadband noise reduction of up to 25dB<sup>6</sup>. For the more complex geometries, the main landing gear with proper porous fairings and hubcaps exhibited a lower noise level by more than 3EPNdB, and the total aircraft noise was reduced by 0.8EPNdB<sup>7</sup>.

Numerical simulations of noise reduction by the turbulence screens are needed to better understand the control mechanism and speed up their applications in real airplane. However, the sizes of wire or hole are generally two or four orders smaller than the real landing gear. It is almost impossible to resolve the geometries, but only to be modelled in simulations. Okolo et al.<sup>8,9</sup> modeled the turbulence screens as flow and noise control methodology, through adding a body force based on the improved delayed detached eddy simulation (IDDES) model. Terracol et al.<sup>10</sup> developed a screen model through their direct numerical simulation data and applied it to the tandem cylinders. However, the effects of turbulence screen on the near-field flows and far-field noise are needed to deeply investigate.

In this paper, a screen model is introduced, validated and applied to control the flows past the tandem cylinders. The turbulence modeling method is IDDES. The emphasis is investigating the effects of turbulence screen location on the changes of the near-field flows and far-field noise.

## 2. Numerical methods

### 2.1 Turbulence screen model

Many experimental and analytic studies have been performed to investigate the aerodynamic characteristics of turbulence screens<sup>11</sup>. In the analytic researches, the screens are usually supposed to be two dimensional (2-D). Figure 1 presents a turbulence screen, specified by the wire diameter  $d$  and spacing  $s$ . The porosity  $\beta$  is defined as  $\beta = (1 - d/s)^2$ . The air approaches the screen with incident angle  $\theta_1$  and flows away with angle  $\theta_2$ .

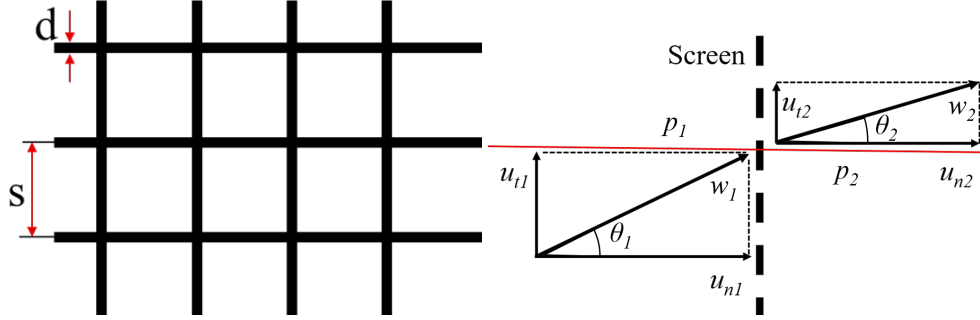


Figure 1: A representation of turbulence screen

According to the previous studies, the effects of turbulence screens on the flow can be categorized into three aspects: resistance, deflection and turbulence alteration. In this paper, the third one is omitted.

The resistance coefficient at approach angle  $\theta_1$  is defined by  $K = (p_1 - p_2) / 0.5\rho w_1^2$ .  $p_1$  and  $p_2$  are the pressure before and after the screen.  $\rho$  is the density;  $w_1$  is the magnitude of approaching velocity. According to the Roach,<sup>12</sup> the  $K$  at  $\theta_1 = 0^\circ$  can be written as:

$$K_0 = \left( 0.52 + \frac{66}{\text{Re}_d^{4/3}} \right) \left( \frac{1 - \beta^2}{\beta^2} \right) \quad 40 < \text{Re}_d < 10^5 \quad (1)$$

where  $\text{Re}_d$  is the Reynolds number based on the wire diameter. Then, the  $K$  can be calculated through  $K = K_0 \cos^2 \theta_1$ .

Gibbins<sup>13</sup> derived an analytical expression of the deflection for "small values of  $K$ ":

$$\frac{\tan \theta_2}{\tan \theta_1} = \left[ \left( \frac{K}{4} \right)^2 + 1 \right]^{1/2} - \frac{K}{4} \quad (2)$$

It has been examined by the results of Taylor et al.<sup>14</sup> in a large range of  $K$  and  $\theta_1$ .

### 2.2 Implementation in the N-S equations

The near-field flows are simulated by solving the compressible N-S equations, based on our in-house code UNITS, which is a density-based solver using the finite volume method on basis of multi-block structured grids. Its performances in predicting unsteady turbulence at high Reynolds number have been demonstrated by several cases, including the tandem cylinders<sup>15</sup>, a rudimentary landing gear<sup>16</sup>, cavities<sup>17</sup>, and a wind turbine airfoil<sup>18</sup> near stall.

The turbulence screens are modeled by adding source terms into the right hand side of momentum equations:

$$\frac{\partial (\rho u_i)}{\partial t} + \frac{\partial (\rho u u_j)}{\partial x_j} = -\frac{\partial p}{\partial x_i} + \frac{\partial}{\partial x_j} \left( \mu \frac{\partial u_i}{\partial x_j} \right) + S_i \quad (3)$$

where  $x_i$  are the Cartesian coordinates and  $u_i$  are the velocity components. For simplification, the  $S_i$  are derived in 2-D. The screen is assumed to be planar and normal to the  $x$  direction.  $S_i$  are expressed as:

$$\begin{bmatrix} S_1 \\ S_2 \\ S_3 \end{bmatrix} = \begin{bmatrix} -K_0 \times 0.5\rho|u|u/h \\ -\rho|u|v(1 - \tan \theta_2 / \tan \theta_1) / h \\ 0 \end{bmatrix} \quad (4)$$

where  $h$  is the thickness of the screen zone in the simulations. To ensure the robustness of simulations, the  $S_i$  are multiplied by a distribution function  $f(l) = 2(1 - 2l/h)$ .  $l$  is the distance from the center plane of the screen zone.

The unsteady near-field flows and turbulence structures are numerically predicted by IDDES model<sup>19</sup>, based on the Menter's shear-stress transport (SST) turbulence model<sup>20</sup>. This advanced RANS-LES hybrid model couples the wall-modeled LES and DDES. More details of this method can be found in reference<sup>16</sup>.

The inviscid flux is discretized by the symmetric total variation diminishing (STVD) scheme<sup>18</sup>, which includes the 4<sup>th</sup> order central flux with the diffusion of Roe through 5<sup>th</sup> order WENO interpolation. Moreover, the original STVD scheme is much more dissipative and its dissipation must to be effectively reduced. According to our previous researches<sup>15</sup>, only the advanced turbulence simulation models are not enough. The high-order adaptive dissipation scheme is also necessary. The scheme acts as the original STVD scheme in the irrotational region, near the wall, far-field boundary, or the shock wave and it acts as the central scheme with very small dissipation in the region dominated by the turbulence. The viscous fluxes are calculated by the 2nd order central scheme. The low-upper symmetric Gauss-Seidel method with Newton-like sub-iterations is implemented, which can achieve 2<sup>nd</sup> order accuracy in time.

### 3. Validation

In this section, several cases are applied to validate our turbulence screen model, comprehensively, including an infinite screen, finite screen, and a windbreak.

#### 3.1 Flow through an infinite screen

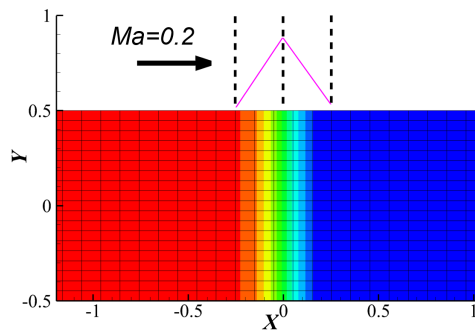


Figure 2: Computational domain and setup for an infinite screen

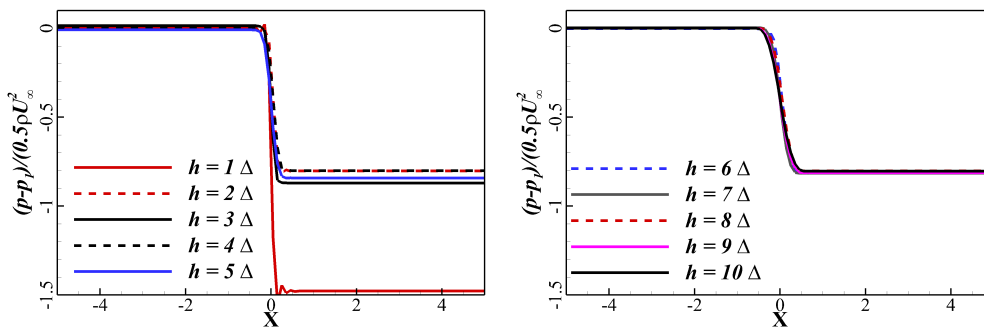


Figure 3: Pressure drops for different  $h$

For the flow passing an infinite screen, the momentum perpendicular to the turbulence screen remains the same, due to mass conservation. Therefore, the pressure drop can be used to certificate the screen model for flow resistance. The computational domain and setup for the infinite screen are shown in Figure 2. Different thicknesses of the screen zone,  $h$ , are set to explore their effects. The pressure drop changes are shown in Figure 3, where  $h$  increases from one to ten times of grid scale,  $\Delta$ . It can be observed that when the  $h < 5.0\Delta$ , the computed value varies drastically as the variation of  $h$ . When the  $h$  continues to increase, a pronounced convergence can be achieved. Therefore, for the implementation of turbulence screen model,  $h$  of  $10\Delta$  is recommended.

## MODELING TURBULENCE SCREEN

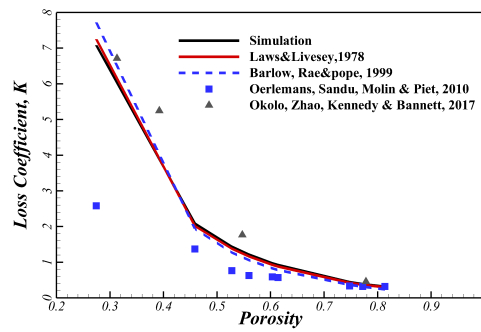
Figure 4: Relationship between the  $K$  and  $\beta$ 

Figure 4 presents the change of loss coefficient,  $K$ , with the porosity,  $\beta$ . For comparison, the empirical equations from the Laws et al.<sup>11</sup>, Barlow et al.<sup>21</sup> and measurements from Oerlemans et al.<sup>6</sup>, Okolo et al.<sup>9</sup> are also plotted together. The two empirical functions perform very similar. While the two results from the measurements separate with each other, especially for the very low porosity. As the porosity increases, the two measurements get closer. When  $\beta > 0.7$ , the empirical functions agree well with the measurements. When  $\beta < 0.4$ , the empirical functions provide good agreements with the measurements of Okolo et al. When  $0.4 < \beta < 0.7$ , the empirical functions lie between the two measurements. Our simulations almost coincide with those of the two empirical functions. Therefore, the choice of this resistance model (Equ.1) is reasonable.

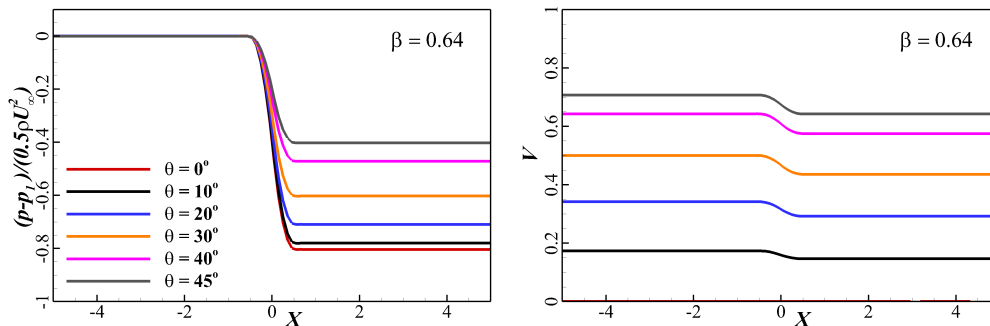


Figure 5: Comparisons of pressure and vertical velocity changes for different incident angles

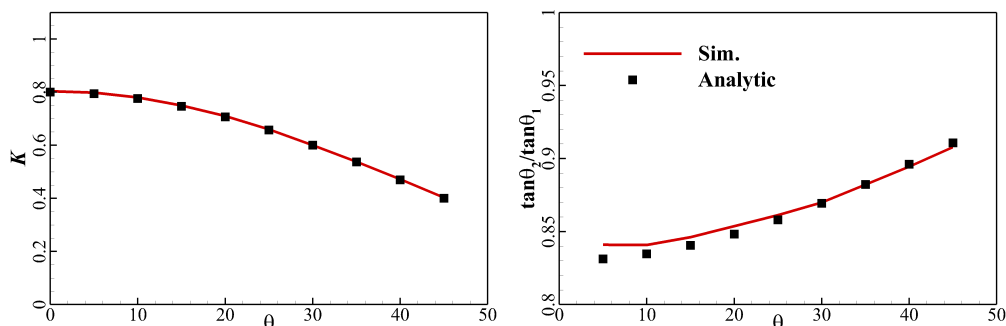


Figure 6: Comparisons of simulation results and analytical values for different incident angles

The deflection coefficient function (Equ.2) is tested by changing the incident angle. The pressure and vertical velocity changes for different incident angles are shown in Figure 5. From this figure, the pressure drop across the screen reduces as the incident angle increases. A drop of vertical velocity is observed and the value depends on the incident angle, as expected. Then, the resistance and deflection coefficients are extracted and demonstrated in Figure 6. The Equ.1 and Equ.2 are well reproduced by our simulations.

### 3.2 Flow through a finite screen

For a real turbulence screen in applications, the screen size is limited. In this section, a finite screen is simulated to evaluate the effects of screen with limited size. The computational grids are shown in Figure 7, with edge of  $L$ . In order to study the damping effect of screens on the existing turbulence, the freestream turbulence level of 1.4% is imposed at upstream of the screen. The turbulence fluctuations are synthesized by the random flow generation technique (RFG) developed by Smirnov et al.<sup>22</sup>. The main advantage of this method is to keep a small number of parameters to set, which fits well the requirements of industrial applications<sup>23</sup>. In our simulations, the number of the random sampling is set as 1000 and the turbulence length scale is  $0.1L$ .

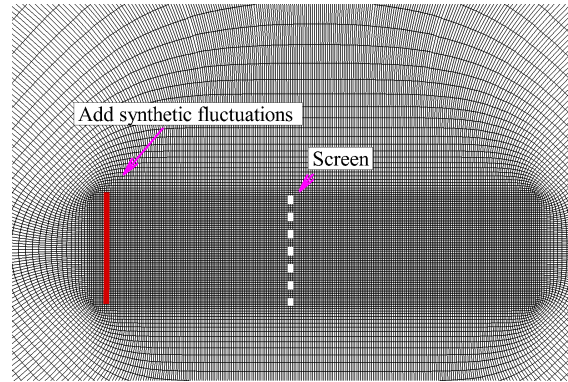


Figure 7: The computational grid for the finite screen

The flow visualization of  $K = 0.6$  and distributions of  $U/U_\infty$  are presented in Figure 8. The flow across the screen is decelerated, while the flow around the screen is accelerated. A shear layer is formed between the fast freestream and slow wake of screen. On the right, it can be observed that the low-velocity region is very long and the velocity will be decreased by the increase of  $K$ .

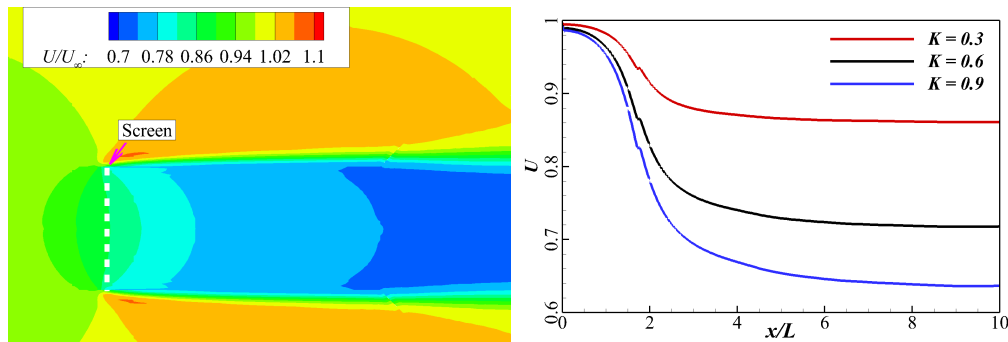


Figure 8: The comparisons of the mean streamwise velocity

To assess the effect of screen on upstream turbulence, reduction factors are defined as the ratio of turbulence intensity with and without the screen at the same downstream location.

$$f_u = \frac{u_{rms,with-screen}}{u_{rms,without-screen}}, f_v = \frac{v_{rms,with-screen}}{v_{rms,without-screen}} \quad (5)$$

The reduction factors at the downstream of screen from simulations are shown in Figure 9. For comparison, the analytical<sup>14</sup> results of  $f_u$  and empirical function<sup>24</sup> of  $f_v$  are also presented. The present simulations provide good agreements with the theoretical or empirical results without any modification to the turbulence model. This indicates that the turbulence reduction can be achieved by Eqs.1 and 2 in unsteady simulation. The explicit implementation of reduction factors is not necessary.

### 3.3 Flow over a windbreak

The flow past a windbreak, which is very similar with the turbulence screen, has been experimentally tested by Maruyama<sup>25</sup>. This case can be used to validate our screen model. The schematic of the windbreak and computational

## MODELING TURBULENCE SCREEN

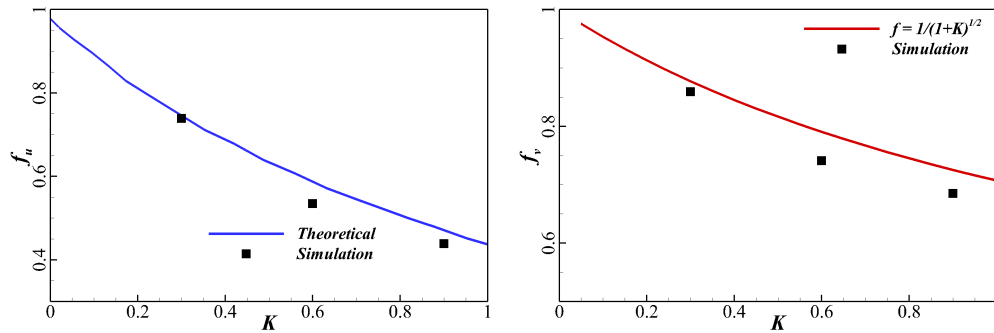
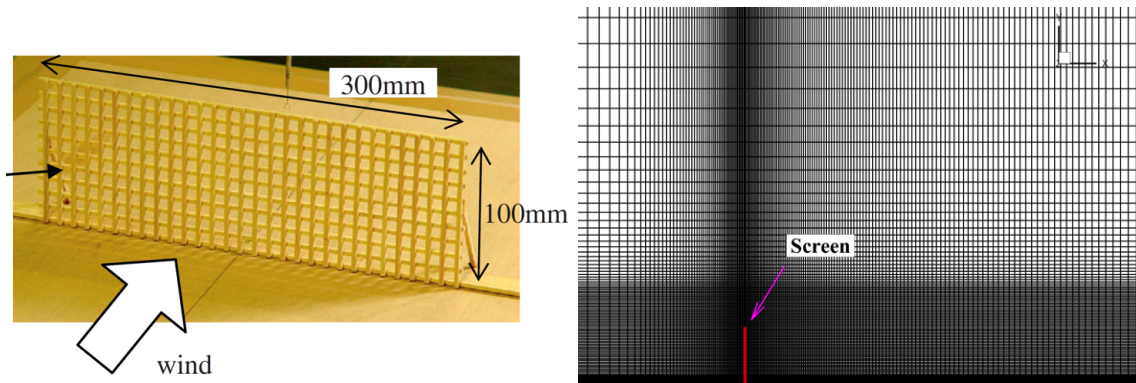


Figure 9: The comparisons of turbulence reduction factors

domain are shown in Figure 10. The turbulence screen (windbreak) has the height,  $H$ , of 100mm. The width-to-height ratio is 3. The grid scale around the screen is about  $0.02H$ . The total cells are about 6.5 million. Steady RANS method is performed and the porosity is set as 0.42 here.

Figure 10: The schematic<sup>25</sup> and computational domain of the windbreak

The results are shown in Figure 11. The numerical streamwise velocity profiles at four stations,  $x/H = -1, 1, 2,$  and 4, agree well with the measurements. Therefore, the present model could capture the reduction of flow speed after the turbulence screen.

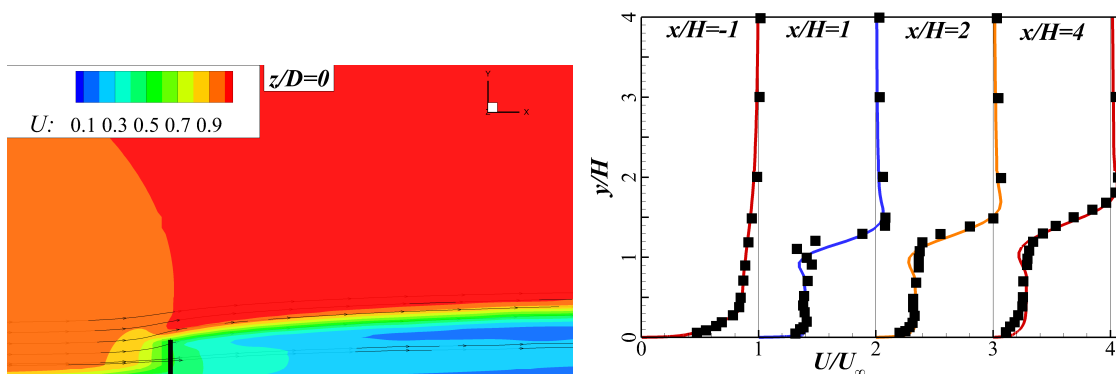


Figure 11: Comparison of streamwise velocity profiles

#### 4. Application to the tandem cylinders

In this section, the turbulence screen model is applied to the tandem cylinders with spacing of  $3.7D$ . The near-field flow and far-field noise have been experimentally tested in Basic Aerodynamic Research Tunnel (BART)<sup>26</sup> and Quiet

Flow Facility (QFF)<sup>27</sup>. In the experiments, the flow speed was  $44\text{m/s}$  and the Reynolds number based on the cylinder diameter,  $Re_D$ , is  $1.66 \times 10^5$ . A transition trip was applied on the windward side of the front cylinder to trigger transition. In another experiment, a trip was even attached on the rear cylinder (azimuthal angle of  $70$  to  $80^\circ$ ) to ensure the flow transition on the rear cylinder<sup>28</sup>. The tandem cylinders both with and without control are the test cases in IMAGE project. The flows and noise were measured again in Aircraft Strength Research Institute (ASRI), China. In the experiment by ASRI, the flow velocity was  $64\text{m/s}$ . To ensure the same Reynolds number with BART and QFF, the diameter of cylinders in ASRI is smaller.

Two types of turbulence screen with the porosity of  $0.79$  and  $0.66$  are used to control the flow and noise. The turbulence screens and their applications in tandem cylinder are shown in Figure 12. Both the two screens are planar with  $1.5D$  width in  $y$  direction. They are all  $10D$  in spanwise direction and their endings are fixed on the wind tunnel wall. The turbulence screens are installed at  $x/D = -1.0$ .

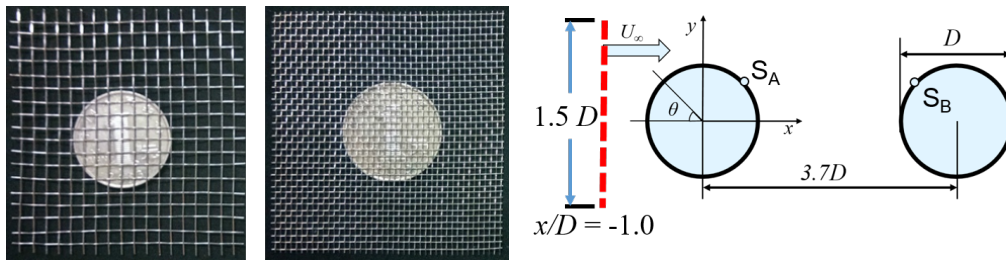


Figure 12: The turbulence screens and application in the tandem cylinders

In the present simulations, the Mach number is  $0.2$  and  $Re_D = 1.66 \times 10^5$ . The porosities,  $0.79$  and  $0.66$ , are the same in the experiment. The flow is thought as full turbulence, without transition on the cylinder surfaces.

The computational grids near the tandem cylinders and the FW-H integral surfaces are presented in Figure 13. To capture the 3-D flow structures, the spanwise length is  $3D$  with uniform grid points. The total cells are about 11 million with cell scale of  $0.02D$  in the gap region. The integral surface (red lines) for the FW-H equation is penetrable and it nearly includes all the noise sources. The cylinder surfaces are treated as no-slip walls. At the far-field boundary, a non-reflection condition is applied. In the spanwise direction, a periodic boundary is adopted. The non-dimensional time step is  $0.01$ , corresponding to about 400 steps in a vortex shedding period. The unsteady information is recorded for  $2^{14}$  time steps to conveniently analyze the unsteady signals, such as the pressure and velocity fluctuations.

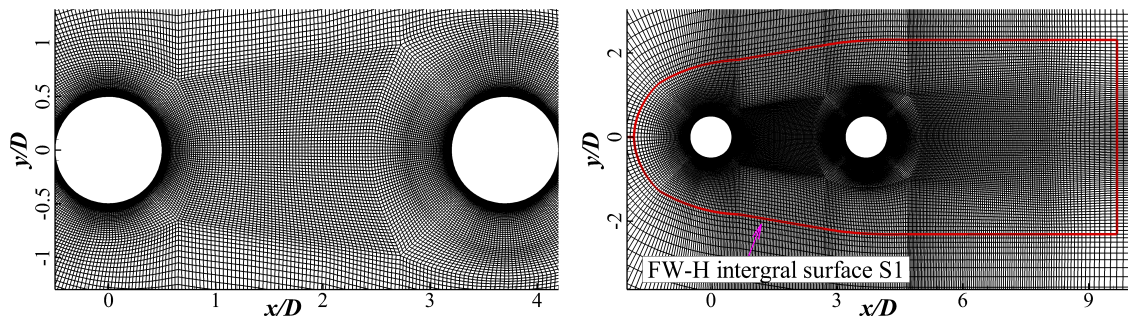


Figure 13: Near-field grids and FW-H integral surface

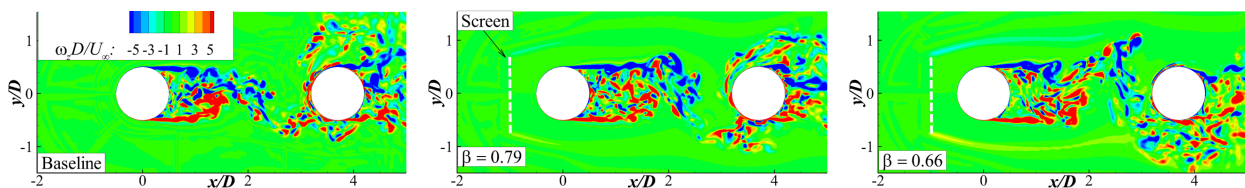


Figure 14: Comparisons of instantaneous vorticity  $\omega_z D / U_\infty$  for the baseline and controlled cases

Figure 14 presents the instantaneous spanwise vorticity ( $\omega_z D / U_\infty$ ) with and without turbulence screens. As expected, a shear layer forms at the edge of the screen. When the porosity is reduced, the shear layer is enhanced. The

## MODELING TURBULENCE SCREEN

baseline and two controlled cases exhibit very similar turbulence structures. It indicates that the vortex shedding from the front cylinder still dominates the flow.

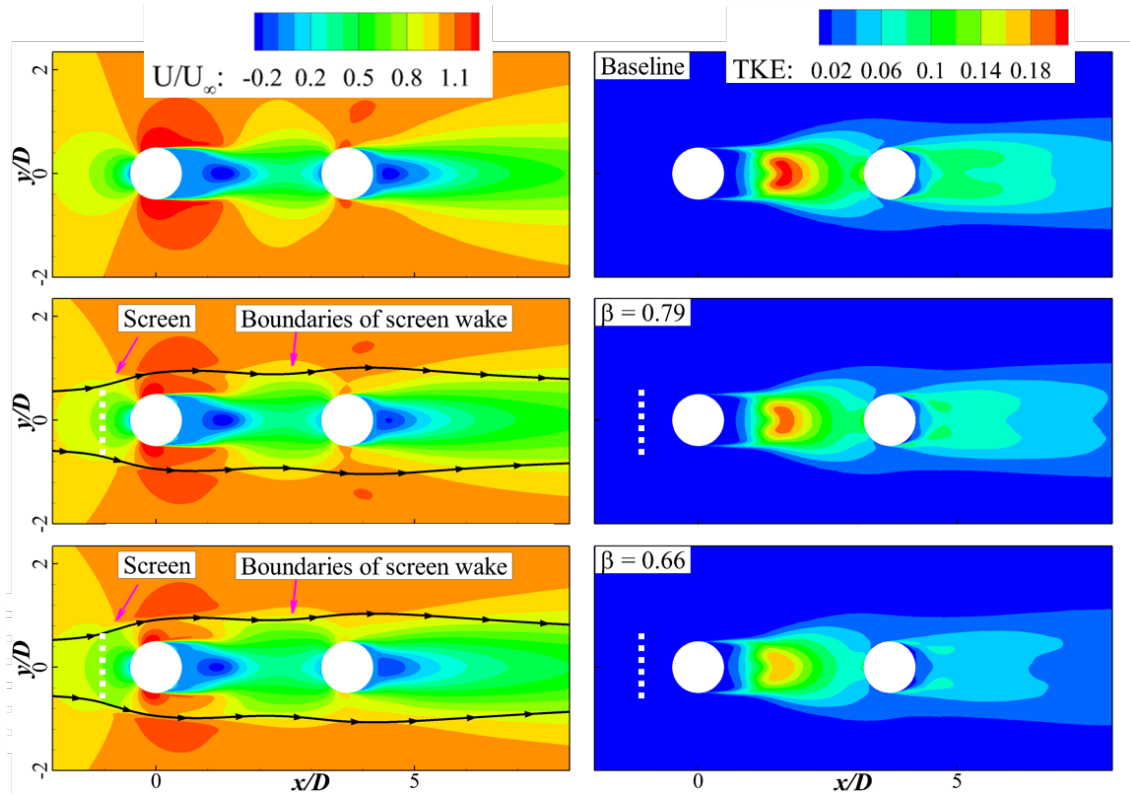


Figure 15: Comparisons of  $U/U_\infty$ , and TKE with and without the screens

The comparisons of  $U/U_\infty$  and resolved turbulent kinetic energy ( $TKE = 0.5(u_{rms}^2 + v_{rms}^2 + w_{rms}^2)$ ) for the baseline and controlled cases are presented in Figure 15. For the controlled case, both cylinders are immersed in the wake of screen and the overall flow speed past the tandem cylinders is reduced. The TKE in the wake of both cylinders is also decreased. When the porosity decreases, the speed of the flow across the two cylinders and TKE are both reduced. Besides, the turbulence screens have an important effect on the recirculation. The screen with  $\beta$  of 0.66 moves the reattachment point from  $1.72D$  (baseline) to  $1.59D$ . It means that the screen moves the vortex shedding closer to the front cylinder.

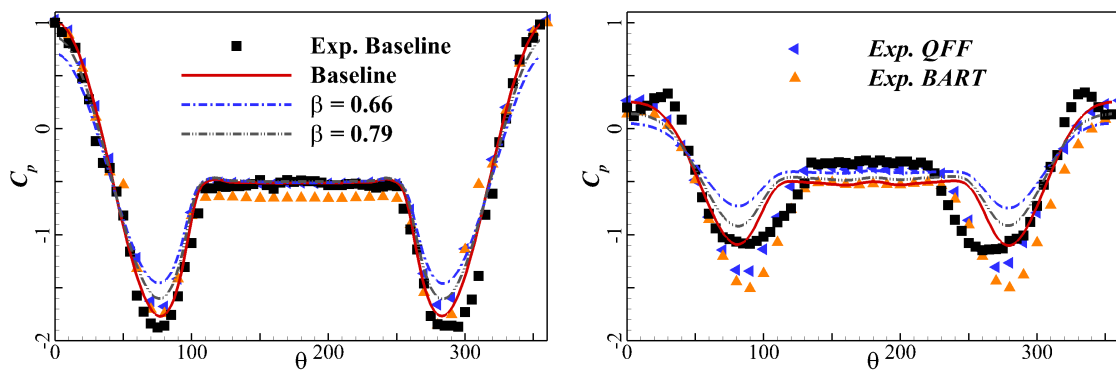


Figure 16: Comparisons of  $C_p$  on the cylinder surfaces (left:front; right:rear)

Figure 16 presents the comparisons of  $C_p$  with and without the control of screens. For comparison, the experimental results for the baseline from the ASRI(baseline), BART, and QFF are also plotted. The simulation results agree well with those of the experiments. The  $C_p$  at the stagnation points of the two cylinders are both decreased by reducing the flow speed. When the porosity is smaller, the absolute values of  $C_p$  at the stagnation point and negative peaks are

also smaller. The turbulence screens have little effects on the  $C_p$  for the leeward side of the front cylinder. On the rear cylinder, the absolute values of  $C_p$  decrease with the decrease of the porosity.

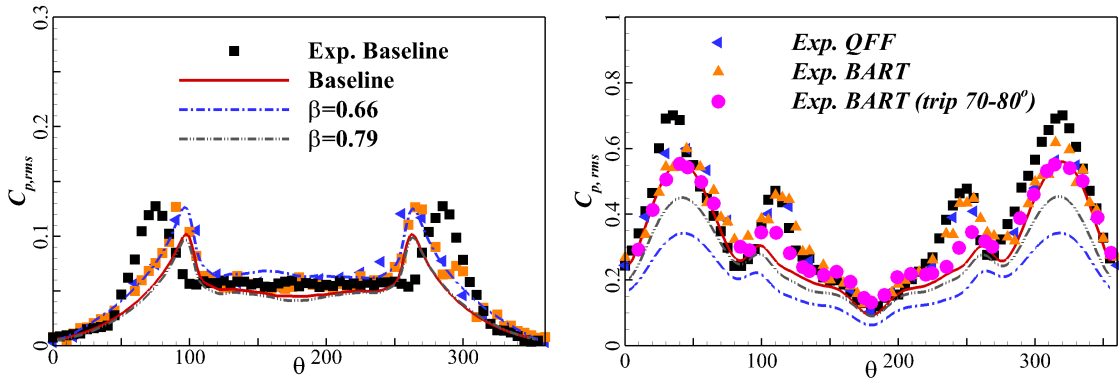


Figure 17: Comparisons of  $C_{p,rms}$  on the front and rear cylinder surfaces

For  $C_{p,rms}$  (shown in Figure 17), the good agreements with the measurements are also observed. The effects of screens on the front and rear cylinders are different, even contrary. On the front cylinder, the  $C_{p,rms}$  of baseline are almost the smallest and nearly similar with those by porosity of 0.79. The pressure fluctuations become larger with the decrease of porosity. On the rear cylinder, the  $C_{p,rms}$  are mainly caused by the interaction with the front cylinder wake. The wake from the front cylinder is reduced by the screens owing to the reduction of flow speed. As a result, the  $C_{p,rms}$  on the rear cylinder are greatly reduced.

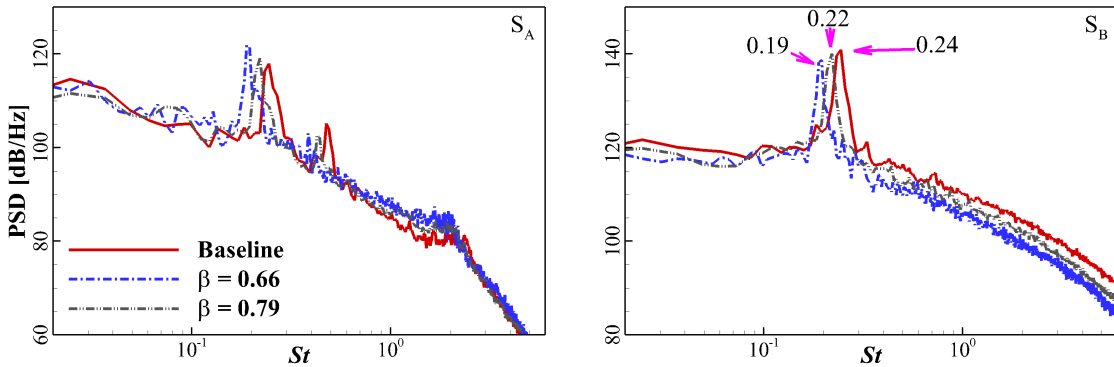


Figure 18: PSDs for sample  $S_A$  and  $S_B$

The PSDs of pressure at samples,  $S_A$  and  $S_B$ , are shown in Figure 18. The primary frequency, the non-dimensional Strouhal number ( $St$ ) at  $S_A$  is the same as that of  $S_B$  for the baseline and controlled case. At the same time, the primary frequencies by the turbulence screens are reduced and the smaller porosity results in lower primary frequency. The dominant frequencies for  $\beta$  of 0.66 and 0.79 are 0.19 and 0.22, respectively, comparing to 0.24 of the baseline case. The effects on PSD magnitudes are similar with those of  $C_{p,rms}$ .

The comparisons of the far-field noise between the simulations and the QFF are shown in Figure 19. In QFF experiment, the microphones were mounted at a constant distance of  $26.67D$  from the traverse center of rotation  $(x/D, y/D) = (9.11, -2.4)$ , in the mid-span section. The PSDs of three microphones placed at  $S_C$  ( $-8.33D, 27.815D$ ),  $S_D$  ( $9.11D, 32.49D$ ), and  $S_E$  ( $26.55D, 27.815D$ ) are also compared. The results agree with the measurements very well for the OASPL (overall sound pressure level) and PSDs at the three microphones.

The comparisons of far-field noise between simulation and the ASRI experiment, where the microphones are placed with distance of  $37.5D$ , are shown in Figure 20. From the comparisons, the differences of amplitude between the measurements and simulations are small. The distinct difference is the frequency, especially the dominant one.

For the baseline case without control, the dominant frequency of the measurements from ASRI is 0.19. It is different from those from BART of 0.235, QFF of 0.231 and present simulation of 0.24. This difference is possibly caused by the lack of effective transition trips on the windward surface of front cylinder. For the controlled case with the screen porosity of 0.79, the dominant frequency of present method decreases to 0.22 owing to the reduced impinging speed. At the same time, the experimental dominant frequency increases to 0.20. The increase of dominant frequency

## MODELING TURBULENCE SCREEN

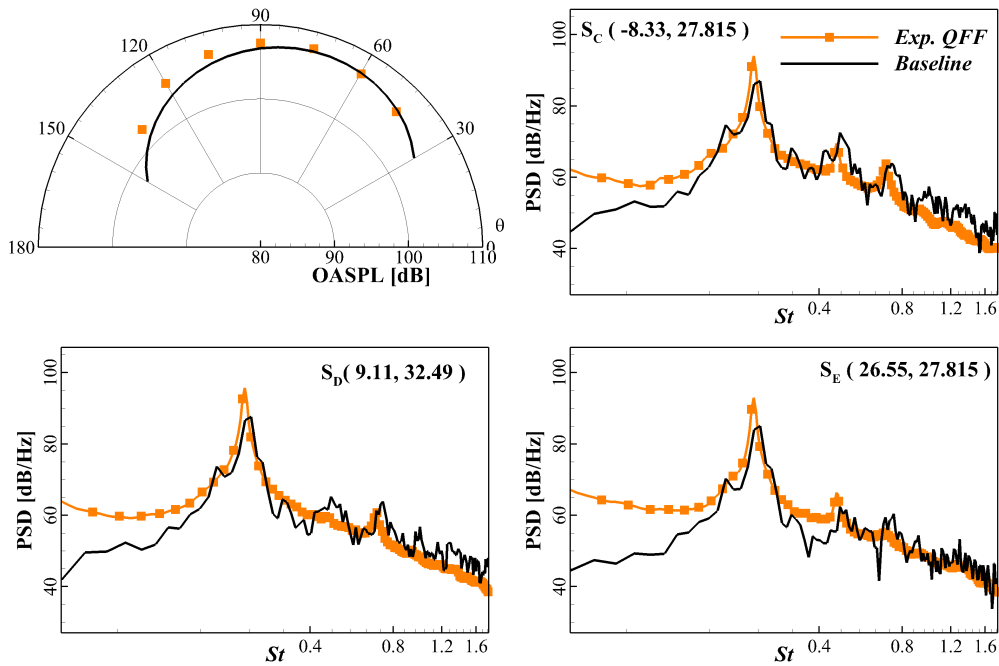


Figure 19: Comparisons of the baseline noise between the simulation and the QFF experiment

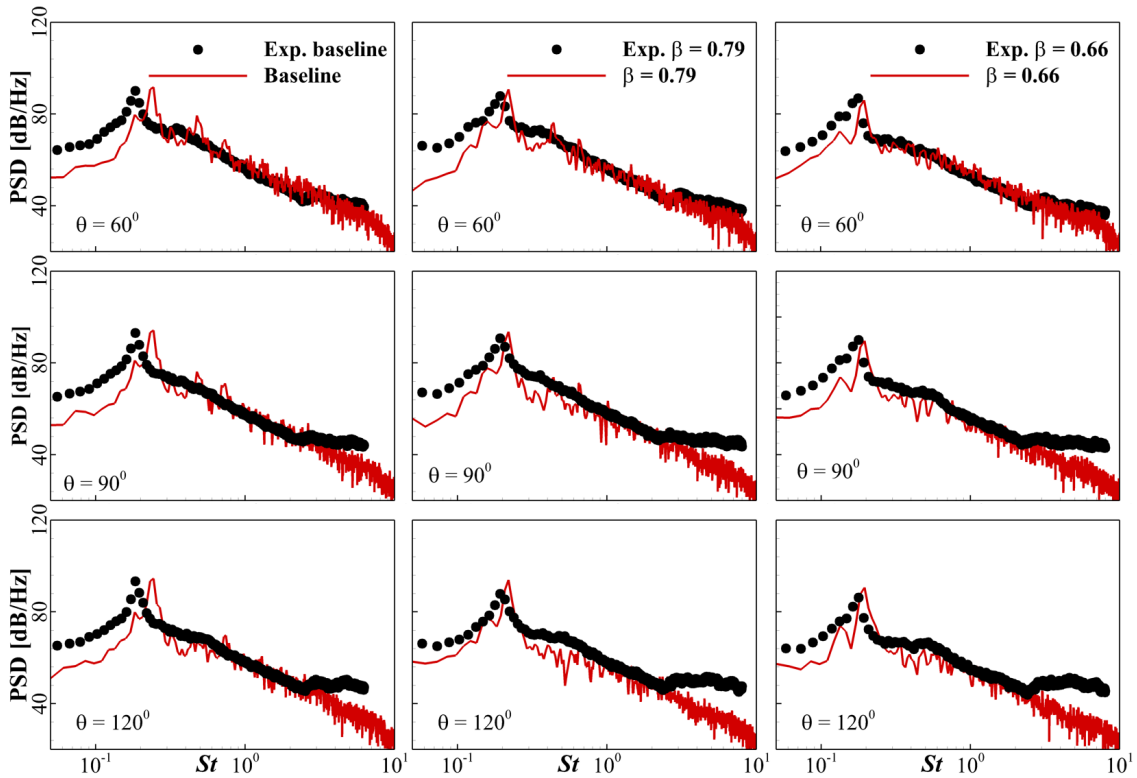


Figure 20: Comparisons of PSD at microphone locations for the baseline and controlled cases

in experiment is possibly caused by the screen wake, which can accelerate the transition on the windward surface of front cylinder. The dominant frequency of turbulent cylinder is a little larger than that of laminar one.

As the screen porosity decreases to 0.66, the dominant frequencies for the simulation and experiment are 0.19 and 0.174, respectively. For this case, the effect of reduced flow speed by the screen on the dominant frequency exceeds that of the transition on the windward side.

Overall, the numerical simulations present reasonably good agreements with the measurements, although some differences exist. However, it is very difficult to find the exact causes of these differences, due to the lack of detailed flow quantities from the experiments.

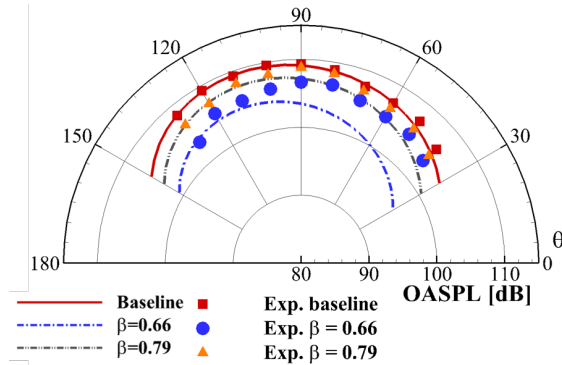


Figure 21: Comparisons of OASPL for the baseline and controlled cases

The comparisons of OASPL directivity are shown in Figure 21. It can be observed that both the turbulence screens provide a substantial noise reduction. As the screen porosity is smaller, the OASPL also becomes smaller. At the emission angle of  $120^\circ$ , the screen with  $\beta$  of 0.66 can achieve a maximal OASPL reduction of 4.9dB. The minimum OASPL reduction is 1.8dB by the screen with  $\beta$  of 0.79. The reduction of experiments are 3.9 dB and 2.2 dB. For smaller emission angle, the difference between the simulations and experiments becomes larger.

According to Oerlemans et al.<sup>6</sup> and Boorsma et al.<sup>29,30</sup>, a noise increase in the high-frequency range is always caused by the self-noise of turbulence screen, which is not considered in our simulation, owing to the damping screen model. In practice, the noise increase at high-frequency range is not very important, because of the A-weighting and atmospheric attenuation in these frequencies.

## 5. Conclusion

Turbulent screens have been numerically modelled by introducing the source terms to the momentum equations of N-S equations. Then, this model is applied to the tandem cylinders as a flow and noise control methodology device. The near-field flows are predicted by the IDDES. The far-field noise is calculated by solving the FW-H equation.

The screen model is validated by an infinite size screen with different incident angles and porosity, a finite screen with freestream turbulence, a windbreak installed on the ground. After comparing the numerical results with the analytic results or measurements, good agreements are achieved, including the resistance and deflection coefficients, turbulence reduction factors, time-averaged velocities. Through these cases, the present screen model can predict the effects of turbulence screen on near-field flow.

Then, the turbulence screen model is applied to control the noise from the tandem cylinders. The screen could decrease the near-field pressure fluctuations and far-field noise by reducing the flow speed after the screen. The dominant frequency become lower and the noise reduction increases when the porosity decreases from 0.79 to 0.66. The screen with porosity of 0.66 achieves a maximum reduction of 4.9 dB at the emission angle of  $120^\circ$ . Meanwhile, at the porosity of 0.79, a noise reduction of only 1.8 dB is obtained.

## 6. Acknowledgments

This work was supported by the EU-China cooperation IMAGE project (Grant No 688971) and the National Natural Science Foundation of China (Grant No. 11772174 and 91852113). IMAGE (Innovative Methodologies and technologies for reducing Aircraft noise Generation and Emission) is an EU-China collaborative project between the European team (Chalmers, AGI, CFDB, CIMNE, KTH, NLR, NUMECA, ONERA, RWTH-Aachen, TU-K, UPM, and VKI) and Chinese team (ASRI, ACAE, ARI, BARTRI, BUAA, FAI, IMech, NPU, and THU).

## References

- [1] W. Dobrzynski and H. Buchholz. Full-scale noise testing on airbus landing gears in the german dutch wind tunnel. In *3rd AIAA/CEAS Aeroacoustics Conference*, AIAA paper 97-1597-CP, Atlanta,GA, U.S.A., May 1997. doi:10.2514/6.1997-1597.
- [2] W. Dobrzynski, L. Chow, P. Guion, and D. Shiells. A european study on landing gear airframe noise sources. In *6th Aeroacoustics Conference and Exhibit*, AIAA paper 2000-1971, Lahaina, HI,U.S.A., June 2000. doi:10.2514/6.2000-1971.
- [3] J. F. Piet, R. Davy, G. Elias, H. Siller, L. Chow, C. Seror, and F. Laporte. Flight test investigation of add-on treatments to reduce aircraft airframe noise. In *11th AIAA/CEAS Aeroacoustics Conference*, AIAA paper 2005-3007, Monterey, California, May 2005. doi:10.2514/6.2005-3007.
- [4] K. Boorsma, X. Zhang, and N. Molin. Landing gear noise control using perforated fairings. *Acta Mechanica Sinica*, 26(2):159–174, 2010.
- [5] K. Andrzej and L. Joanna. Experimental and modelling study on flow resistance of wire gauzes. *Chemical Engineering and Processing: Process Intensification*, 48(3):816–822, 2009.
- [6] S. Oerlemans, C. Sandu, N. Molin, and J.-F. Piet. Reduction of landing gear noise using meshes. In *16th AIAA/CEAS Aeroacoustics Conference*, AIAA paper 2010-3972, Stockholm, Sweden, June 2010.
- [7] M. Smith, L. Chow, and N. Molin. Control of landing gear noise using meshes. In *16th AIAA/CEAS Aeroacoustics Conference*, AIAA paper 2010-3974, Stockholm, Sweden, June 2010.
- [8] P. N. Okolo, K. Zhao, J. Kennedy, and G. J. Bennett. Mesh screen application for noise reduction of landing gear strut. In *22nd AIAA/CEAS Aeroacoustics Conference*, AIAA paper 2016-2845, Lyon, France, June 2016.
- [9] P. N. Okolo, K. Zhao, J. Kennedy, and G. J. Bennett. Numerical modeling of wire screens for flow and noise control. In *23rd AIAA/CEAS Aeroacoustics Conference*, AIAA paper 2017-3700, page 3700, Denver, Colorado, June 2017.
- [10] M. Terracol and E. Manoha. Development of a wire mesh screen model for unsteady simulation of noise reduction devices, with application to the tandem cylinder configuration. In *2018 AIAA/CEAS Aeroacoustics Conference*, AIAA paper 2018-3473, Atlanta, Georgia, June 2018.
- [11] E. Laws and J. Livesey. Flow through screens. *Annual Review of Fluid Mechanics*, 10(1):247–266, 1978.
- [12] P. E. Roach. The generation of nearly isotropic turbulence by means of grids. *International Journal of Heat and Fluid Flow*, 8(2):82–92, 1987.
- [13] J. G. Gibbings. The pyramid gauze diffuser. *Ingenieur-Archiv*, 42:225–233, 1973.
- [14] G. Taylor, G. Batchelor, H. Dryden, and G. Schubauer. The effect of wire gauze on small disturbances in a uniform stream. *The Quarterly Journal of Mechanics and Applied Mathematics*, 2(1):1–29, 1949.
- [15] Z. X. Xiao, J. Liu, J. B. Huang, and S. Fu. Numerical dissipation effects on massive separation around tandem cylinders. *AIAA Journal*, 50(5):1119–1136, 2012.
- [16] Z. X. Xiao, J. Liu, K. Y. Luo, J. B. Huang, and S. Fu. Investigation of flows around a rudimentary landing gear with advanced detached-eddy-simulation approaches. *Aiaa Journal*, 51(1):107–125, 2013. Times Cited: 27  
18th AIAA/CEAS Aeroacoustics Conference / 33rd AIAA Aeroacoustics Conference Jun 04-06, 2012 Colorado Springs, CO Aiaa; ceas 0 38.
- [17] K. Y. Luo, W. Q. Zhu, Z. X. Xiao, Z. Weng, L. D. Deng, D. G. Yang, and J. Liu. Investigation of spectral characteristics by passive control methods past a supersonic cavity. *AIAA Journal*, 56(7):2669–2686, 2018.
- [18] J. Liu, W. Q. Zhu, Z. X. Xiao, H. S. Sun, Y. Huang, and Z. T. Liu. Ddes with adaptive coefficient for stalled flows past a wind turbine airfoil. *Energy*, 161:846–858, 2018.
- [19] M. L. Shur, P. R. Spalart, M. K. Strelets, and A. K. Travin. A hybrid rans-les approach with delayed-des and wall-modelled les capabilities. *International Journal of Heat and Fluid Flow*, 29(6):1638–1649, 2008.

- [20] F. R. Menter. Two-equation eddy-viscosity turbulence models for engineering applications. *AIAA journal*, 32(8):1598–1605, 1994.
- [21] J. B. Barlow, W. H. Rae, A. Pope, and A. Kassae. *Low-Speed Wind Tunnel Testing*. John Wiley and Sons Limited, 2015.
- [22] A. Smirnov, S. Shi, and I. Celik. Random flow generation technique for large eddy simulation and particle dynamics modeling. *Journal of Fluid Engineering*, 123:359–371, 2011.
- [23] J. Verriere, F. Gand, and S. Deck. Zonal detached eddy simulations of a dual-stream jet: Turbulence rate sensitivity. *AIAA Journal*, 55(8):2503–2521, 2017. Verriere, Jonas Gand, Fabien Deck, Sebastien 1533-385x.
- [24] G. B. Schubauer, W. G. Spangenberg, and P. Klebanoff. Aerodynamic characteristics of damping screens. Report NACA-TN-2001, 1950 1950.
- [25] T. Maruyama. Large eddy simulation of turbulent flow around a windbreak. *Journal of Wind Engineering and Industrial Aerodynamics*, 96(10-11):1998–2006, 2008.
- [26] L. Jenkins, M. Khorrami, M. Choudhari, and C. McGinley. Characterization of unsteady flow structures around tandem cylinders for component interaction studies in airframe noise. In *11th AIAA/CEAS Aeroacoustics Conference*, AIAA paper 2005-2812, Monterey, California, May 2005.
- [27] F. Hutcheson and T. Brooks. Noise radiation from single and multiple rods configurations. In *12th AIAA/CEAS Aeroacoustics Conference (27th AIAA Aeroacoustics Conference)*, AIAA paper 2006-2629, Cambridge, Massachusetts, May 2006.
- [28] D. Neuhart, L. Jenkins, M. Choudhari, and M. Khorrami. Measurements of the flowfield interaction between tandem cylinders. In *15th AIAA/CEAS Aeroacoustics Conference*, AIAA paper 2009-3275, Miami, Florida, May 2009.
- [29] K. Boorsma, X. Zhang, and N. Molin. Perforated fairings for bluff body noise control. In *13th AIAA/CEAS Aeroacoustics Conference*, AIAA paper 2007-3462, Rome, Italy, May 2007.
- [30] K. Boorsma, X. Zhang, N. Molin, and L. C. Chow. Bluff body noise control using perforated fairings. *AIAA Journal*, 47(1):33–43, 2009.